Article:

Driver, L., Robertson, M.E., Lucas, D.I. et al. (Accepted: 2026) Experimental and Numerical Analysis of Surrogate Optimized de Laval Nozzles in Low-Temperature Supersonic Flows. Physics of Fluids. ISSN: 1070-6631 (In Press)

Experimental and Numerical Analysis of Surrogate Optimized de Laval Nozzles in Low-Temperature Supersonic Flows

Luke Driver,[1] Madeleine E. Robertson,[2] Daniel I. Lucas,[2] Lok Yiu Wu,[2] Nik Kapur,[3] Julia H. Lehman,[2] Dwayne E. Heard,[4] and Gregory N. de Boer[3, a)]

[1)] *School of Computing, University of Leeds, EPSRC CDT in Fluid Dynamics, Woodhouse Lane, Leeds LS2 9JT, United Kingdom*

[2)] *School of Chemistry, University of Birmingham, Edgbaston, Birmingham B15 2TT, United Kingdom*

[3)] *School of Mechanical Engineering, University of Leeds, Woodhouse Lane, Leeds LS2 9JT, United Kingdom*

[4)] *School of Chemistry, University of Leeds, Woodhouse Lane, Leeds LS2 9JT, United Kingdom*

(Dated: 4 August 2026)

[a)] Electronic mail: G.N.deBoer@leeds.ac.uk

I. INTRODUCTION

This supplementary information presents the mathematical formulation of the optimal Latin hypercube sampling strategy, regression Kriging, and feed-forward neural network (FFNN) surrogate models. It also documents the preliminary design optimisation studies used to define optimisation constraints and to reduce the design space a priori, prior to implementation of the significantly larger nine-dimensional model presented in the main paper.

Specifically, this section includes two-dimensional (2D) shape and pressure studies that were used to constrain the NUBS control points and to define operating pressures based on isentropic flow relationships. In addition, a four-dimensional (4D) model is presented in which both nozzle shape and operating pressure are varied simultaneously. The performance of this 4D model is assessed using both low-fidelity (LF) and high-fidelity (HF) approaches. Comparison of the surrogate predictions demonstrates the superior robustness of the HF-based 4D model relative to the LF approach, motivating its adoption for subsequent optimisation studies.

II. MATHEMATICAL FORMULATIONS

A. Isentropic Nozzle Equations

The Mach number of any nozzle profile can be approximated using the 1D analytical equation:

$$AR(M,\gamma) = \frac{A}{A^*} = \left(\frac{\gamma+1}{2}\right)^{-\frac{\gamma+1}{2(\gamma-1)}} \frac{\left(1+\frac{\gamma-1}{2}M^2\right)^{\frac{\gamma+1}{2(\gamma-1)}}}{M} \tag{1}$$

where A is the local nozzle area and A^* is the nozzle throat area, M is the Mach number and γ is the specific heat ratio of the gas used. The adiabatic equations are as follows:

$$\frac{T_{flow}}{T_{res}} = (1+\frac{\gamma-1}{2}M^2)^{-1}, \tag{2}$$

$$\frac{\rho_{flow}}{\rho_{res}} = (1+\frac{\gamma-1}{2}M^2)^{\frac{-1}{\gamma-1}}, \tag{3}$$

$$\frac{1}{PR_{isen}} = \frac{P_{flow}}{P_{res}} = (1 + \frac{\gamma - 1}{2} M^2)^{\frac{-\gamma}{\gamma-1}}, \tag{4}$$

where T_{flow} and T_{res} is the flow and reservoir temperature, respectively, ρ_{flow} and ρ_{res} is the flow and reservoir density, respectively, and P_{flow} and P_{res} is the flow and reservoir pressure, respectively. To calculate PR_{isen}, Equation 1 can be used to calculate the Mach number of the nozzle, and Equation 4 can be used to approximate the optimal pressure to operate said nozzle.

B. Initial Sampling Plan

The initial sampling plan for the low fidelity model is generated using an optimal Latin hypercube (OLHC), where the Morris Mitchell criterion (Φ_q) is used to maximise the space filling properties of the design points[1]. Using a OLHC approach over a random latin hypercube (RLHC) reduces the likelihood of design point clustering and allows the points to be equally distributed throughout the design space, providing the most information possible with the minimal number of design points for the surrogate modelling process. The Morris-Mitchell criterion is calculated using:

$$\Phi_q(\mathbf{X}) = \left(\sum_{j=1}^{m} J_j d_j^{-q} \right)^{\frac{1}{q}} \tag{5}$$

where $\mathbf{X}$ is the design matrix $\mathbf{X} = \left[\mathbf{x}^{(1)}, \mathbf{x}^{(2)}, ..., \mathbf{x}^{(n)}\right]^T$, with n being the total number of design points. The design matrix contains design points ($\mathbf{x}$), where $\mathbf{x}^{(\mathbf{1})} = [x_1, x_2, ..., x_k]$ and k is the number of dimensions, J is a matrix containing the number of pairs of design points, d is the rectangular distance between all possible pairs of design points and q is a free parameter, that will be chosen through the optimisation procedure. To create the initial low fidelity OLHC using the Φ_q criterion, the design space is populated initially using RLHC with $10k$ points[2]. The location of the design points are moved (while keeping LHC properties) to minimise the Φ_q criterion. This procedure is carried out for $q = [10, 20, 30, 40, 50, 60, 70, 80, 90, 100]$, and the q value that produces the OLHC with the lowest Φ value is used. The Φ_q value is optimized using the evolutionary algorithm by Forrester et al., (2008)[3].

C. Regression Kriging

Kriging is a meta-modeling approach that is used to spatially correlate and interpolate between existing design points to make predictions at unknown locations. Ordinary regression Kriging is used as the underlying model structure is unknown, and can be expressed as the combination of a global trend function and a stochastic process:

$$y(\mathbf{X}) \approx \hat{y}(\mathbf{X}) = f(\mathbf{X}) + Z(\mathbf{X}), \tag{6}$$

where $\hat{y}(\mathbf{X})$ is the Kriging predictor, $f(\mathbf{X})$ is a polynomial function which captures global variations, and $Z(\mathbf{X})$ is a normally distributed Gaussian process with mean zero, variance σ^2, and non-zero covariance. The random process variables are correlated using the Matern 52 correlation function as it is widely used for engineering applications due to its flexibility and high accuracy[4]:

$$\psi(\mathbf{X}^i, \mathbf{X}^l) = \left(1 + \sqrt{5}d + \frac{5d^2}{3} exp(-\sqrt{5}d)\right) \tag{7}$$

where $d = \sqrt{\sum_{l=1}^{k} \phi_k (x_k^{(i)} - x_k^{(l)})^2}$, ϕ_k are the unknown hyper parameters (one for each dimension k), which are found using maximum likelihood estimation (MLE), and are optimized using the default SQP Matlab optimiser, where the bounds for all hyper parameters are set to $-2 \leq \phi \leq 2$ for the adaptive sampling process. Once the adaptive sampling algorithm is complete, the final Kriging model is created with hyper parameter bounds between $-8 \leq \phi \leq 8$ to ensure they do not fall on the bounds during optimisation. From this an n x n correlation matrix can be created from the design points:

$$\mathbf{\Psi} + \lambda\mathbf{I} = \begin{pmatrix} \psi(\mathbf{X}^1, \mathbf{X}^1) + \lambda & \cdots & \psi(\mathbf{X}^1, \mathbf{X}^n) \\ \vdots & \ddots & \vdots \\ \psi(\mathbf{X}^n, \mathbf{X}^1) & \cdots & \psi(\mathbf{X}^n, \mathbf{X}^n) + \lambda \end{pmatrix} \tag{8}$$

where λ is the additional noise parameter and $\mathbf{I}$ is the identity matrix. Regression Kriging (RKR) is an extension of Kriging that relaxes the constraint that the value at a known data point has to equal that value outputted by the Kriging predictor[5]. This is useful for noisy output data, which is evident with the data in this study. The parameter λ is also obtained with the hyper parameters through MLE and is optimized using SQL with the bounds $-5 \leq \lambda \leq 5$. Regression ordinary Kriging predictions of $y(\mathbf{X})$ at unknown locations can be obtained using:

$$\mu(x) = M\alpha + r(\mathbf{X}) \cdot (\Psi + \lambda I)^{-1} \cdot (\mathbf{Y} - F\alpha) \tag{9}$$

where μ is the Kriging prediction mean, F contains information on the polynomial model, M is the model matrix, $\alpha = (F^T(\Psi+\lambda I)^{-1}F)^{-1}F^T(\Psi+\lambda I)^{-1}$ contains the coefficients of the regression function and $r(x)$ is a 1 x n correlation vector between the sample data and the new prediction point. Standard interpolation Kriging can be recovered by setting λ equal to unity. A detailed derivation of both Kriging and regression Kriging can be found in[3]. The implementation of both the regression Kriging and regression cokriging models were carried out using the ooDACE Matlab toolbox[6,7].

D. Neural Network Architecture

A FFNN maps an input vector through a set of layers using[8]:

$$a = f\left(\mathbf{Wp} + b\right) \tag{10}$$

where a is the neural network output, f is the activation function, $\mathbf{W}$ contains the weights of each layer and b are the biases. The activation layers used in this study were the hyperbolic tangent sigmoid (tansig) for the hidden layers, and a linear output layer was used for regression. The final output $\hat{y}(\mathbf{x})$ is compared against the true data $y(\mathbf{x})$, and the network weights are trained by minimising the mean squared error (MSE):

$$MSE = \frac{1}{N}\sum_{i=1}^{N}\left(y_i - \hat{y}_i\right)^2. \tag{11}$$

using the Levenberg-Marquardt backpropagation algorithm available in MATLAB[9]. The weights were updated using validation set and training data, where a 90% and 10% split was used, and a separate test set was used to evaluate global model performance. Alongside updating the weights based on MSE, early stopping based on a non-decreasing validation error was used to avoid over fitting on the training data. The input and output data were normalised between zero and one to improve model performance. To improve the generalisation of the neural networks in this study, an averaging ensemble approach was used[10]. In this study, 40 neural networks were generated using the same dataset, each with different initial weight distributions to account for variability in convergence. The performance of each network was evaluated based on the MSE on the training and validation sets. From these, the top 5 models were selected, and the final neural network surrogate was obtained as a weighted ensemble of these models. The final prediction of the ensemble $\hat{y}(\mathbf{x})$ was computed as:

$$\hat{y}(\mathbf{x}) = \sum_{k=1}^{5} w_k \, \hat{y}_k(\mathbf{x}), \tag{12}$$

where $\hat{y}_k(\mathbf{x})$ denotes the output of the k-th selected neural network and w_k are the weights, where each model was equally weighted, e.g. $w_k = 0.2$.

III. LOW AND HIGH FIDELITY MODEL

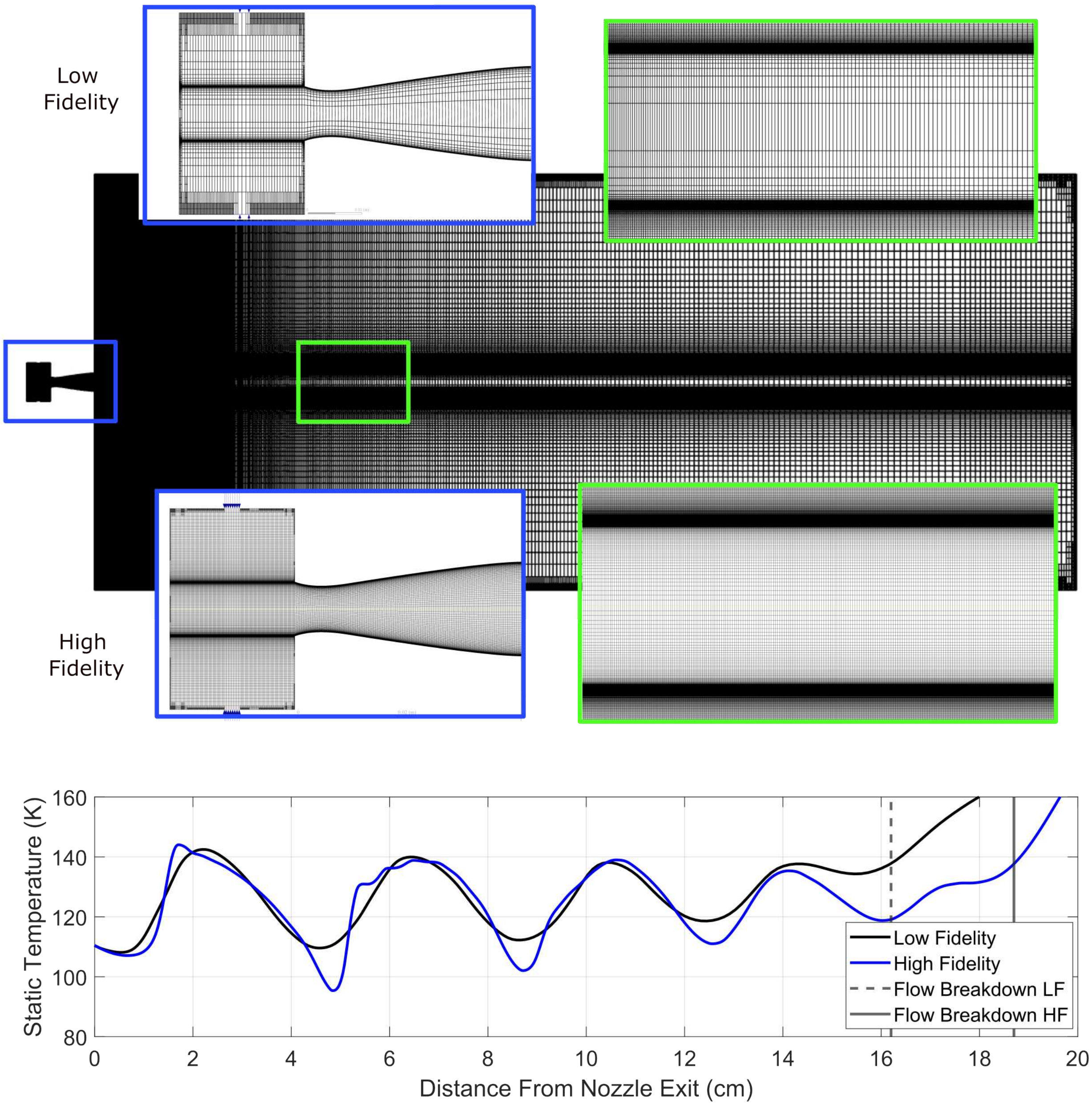

FIG. 1. Comparison between the two meshes used for the high and low fidelity models, with close-ups of the nozzle and immediate flow field (top) and a comparison between the axial static temperature across the jet for both models (bottom).

Alt Text: Computational grid used for the low- fidelity and high-fidelity computations with a comparison of the axial static temperature for each mesh.

In this paper, two levels of models are used, a high fidelity, which uses a grid independent mesh, and a low fidelity which is four times coarser than the high fidelity mesh. Despite this reduction in mesh density, both models employ the same meshing methodology to ensure consistency in the numerical approach. On average, the LF model requires roughly one-tenth of the computational time needed for the HF model using the same computational resources. A comparison between the two meshes with the corresponding axial temperature across a jet generated by an arbitrary nozzle and set of operating conditions is shown in Figure 1.

Both levels of fidelity show very similar shock structures across the jet axis, although the low fidelity model underpredicts both the maximum shock magnitude by ≈ 10 K and the length of the flow by ≈ 2 cm.

IV. ADDITIONAL OPTIMISATION STUDIES

A. 2D Pressure Study

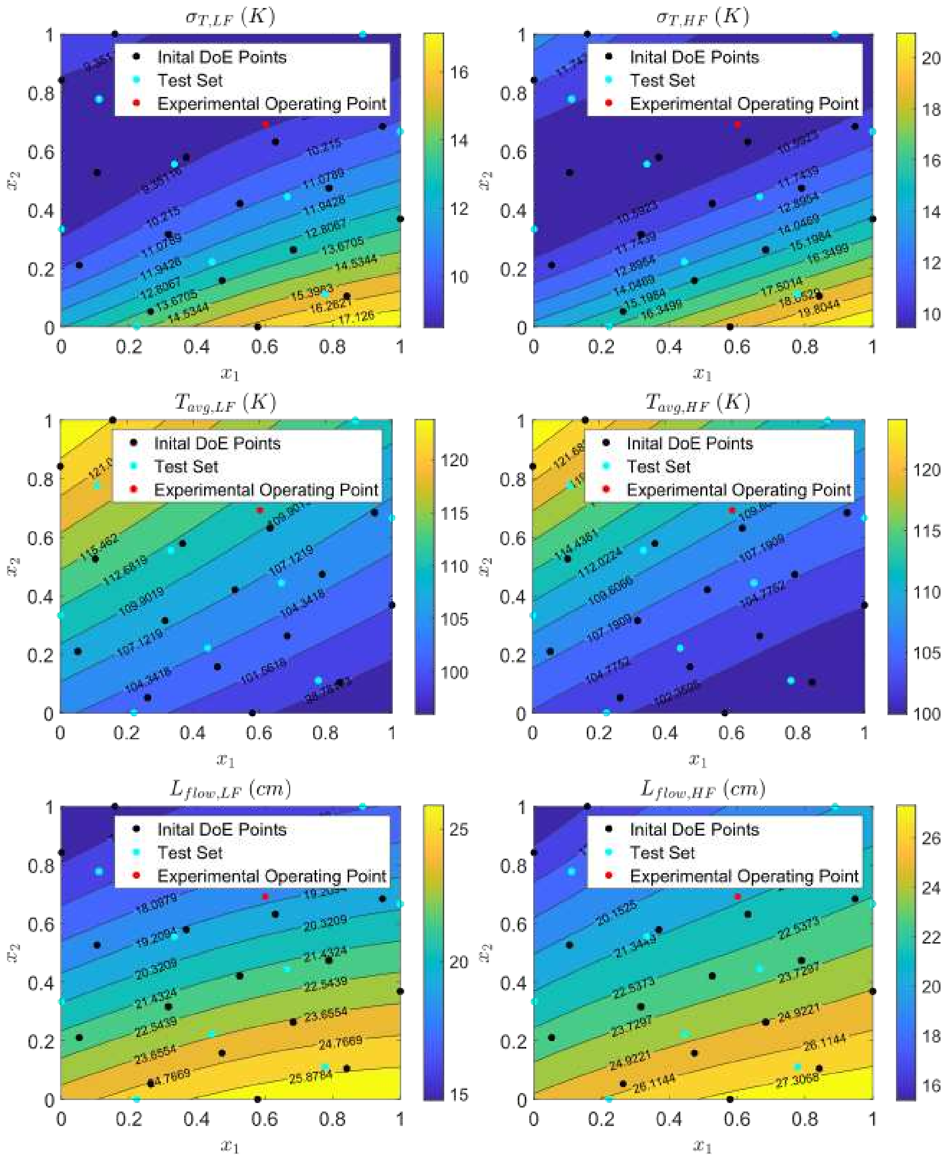

FIG. 2. 2D contours of low fidelity Kriging metamodel (left column) and high fidelity (right column) with locations of sample points for σ_T, M_{avg}, L_{flow} and r_{core}. The red point is the optimal pressure found in the experiment $x_1 = 0.602$ and $x_2 = 0.692$. The test set used to calculate MAE and R^2 of the Kriging model is shown in cyan.

Alt Text: Two-dimensional response surface plot of flow uniformity, jet temperature, and flow length for the high fidelity and low fidelity models showing the design point locations for the initial design of experiment and test set.

In this study, the existing M2.25 nozzle from[11] was used, and the pressure on the inlet and outlet boundaries was varied parametrically using the same optimisation framework. Note that as the design space is 2D, a minimal number of sample points is required for a highly accurate Kriging surrogate model, and hence only one optimisation loop was carried out once the surrogate is built as the GA/GD hybrid always converges to the same minima location. The mathematical formulation of the optimisation problem is as follows:

$$
\begin{aligned}
& \mathbf{x} = [x_1, x_2]^n \quad \text{where } n = 1, 2, ..., N \\
\textbf{Minimise} \quad & f_1(\mathbf{x}) = \sigma_T(\mathbf{x}) \\
\textbf{Subject to} \quad & g_1(\mathbf{x}) = 13 \text{ cm} - L_{flow}(\mathbf{x}) \leq 0 \\
\textbf{where:} \quad & 4000 \text{ Pa} \leq x_1 \leq 6000 \text{ Pa} \\
& 100 \text{ Pa} \leq x_2 \leq 200 \text{ Pa}
\end{aligned}
\tag{13}
$$

where $\mathbf{x}$ is the design matrix, containing N number of samples and $\mathbf{x}^{(1)}$ is the first design point. Note that x_1 and x_2 are the reservoir and chamber pressure, respectively, which are used to set the inlet and outlet boundaries in the CFD case. Alongside understanding the influence of pressure on a specific nozzle, a comparison of a low fidelity and high fidelity approach was conducted, where the data sample points and test set were used for comparison. In this, additional adaptive sampling was not required due to the MAE and R^2 being significantly lower than the termination criteria.

The similarity of the MAE and R^2 values across all cases indicates that both LF and HF models effectively capture the overall trends and topography of the design space.

A comparison between the regression Kriging design space is shown in Figure 2. The low-fidelity (LF) and high-fidelity (HF) surrogate models exhibit comparable mean absolute accuracy for an equal number of samples and share nearly identical topological features across the design space for all kinetic parameters considered. The LF model systematically underpredicts σ_T and L_{flow} relative to the HF model due to under-resolved shocks and increased numerical dissipation associated with the coarser mesh, which shortens the predicted flow length. Predictions of T_{avg} are largely identical between models, with minor discrepancies near the lower-right boundary of the design space, again attributable to unresolved shock structures in the LF case. The correlation coefficients (R^2) between the LF and HF models for σ_T, T_{avg}, L_{flow}, and r_{core} are 0.960, 0.987, 0.977, and 0.982, respectively, with both models identifying a similar region of minimum σ_T. Correlations were computed using R^2 over 1000 identical randomly sampled points. These results demonstrate that the LF approach yields surrogate models of comparable quality and topology to the HF method, while reducing computational cost by approximately an order of magnitude (3 minutes per LF case versus 30 minutes for HF). Following LF optimisation, a final HF evaluation using ACRE can be performed to obtain accurate results suitable for kinetic studies.

Model	Metric	σ_T (K)	T_{avg} (K)	L_{flow} (cm)	r_{core} (mm)
LF Kriging	MAE	0.0260	0.0774	0.0442	0.011
LF Kriging	R^2	0.9997	0.9997	0.9969	0.9897
HF Kriging	MAE	0.0231	0.0605	0.0442	0.0086
HF Kriging	R^2	0.9999	0.9997	0.9997	0.9938

TABLE I. Comparison between Kriging model prediction and test set , MAE refers to mean average error, $NMAE$ refers to normalised mean average error, normalised by the difference between the maximum and minimum value in the test set for comparison. The compute time for the FFNN was less than 5 minutes locally on a 6 core machine, whilst the Kriging model with 10980 samples took $\approx$ 30 hours.

Alt Text: Performance evaluation of low fidelity and high fidelity Kriging surrogate models for flow uniformity, average temperature, flow length and core thickness.

A comparison of the mean absolute error (MAE) and coefficient of determination (R^2) for the low-fidelity (LF) and high-fidelity (HF) Kriging surrogate models and test set are presented in Table I. This shows that Kriging is a very robust technique for accurately capturing trends for low dimensional problems with a smooth design space.

1. *Single Objective Optimisation*

Model	$\mathbf{x}^* = (x_1, x_2)$	$\sigma_T(\mathbf{x}^*)$ (K)	$T_{avg}(\mathbf{x}^*)$ (K)	$L_{flow}(\mathbf{x}^*)$ (cm)
LF Kriging Prediction	[0 0.5600]	8.48	117.02	17.90
LF CFD Evaluation	[0 0.5600]	8.52	117.20	17.81
HF CFD Evaluation	[0 0.5600]	9.78	116.20	19.54
HF Kriging Prediction	[0 0.4540]	9.44	113.66	20.56
LF Kriging Prediction	[0 0.4540]	8.65	114.60	19.01
HF CFD Evaluation	[0 0.4540]	9.50	113.80	20.57

TABLE II. Comparison of Kriging model predictions and CFD results at optima from low fidelity (LF) and high-fidelity (HF) models. Note that the first three rows and last three rows are the global optimal results and corresponding evaluations of the LF and HF models and validation with CFD.

Alt Text: Evaluation of global optima found with the low fidelity and high fidelity approach, where the flow length, average jet temperature and flow length are compared.

The surrogate models were optimized using GA and then refined using GD. Note that only one optimisation run was needed as there was no variability in the global minima found in this instance. Table III shows a comparison of the global optimal obtained for both the LF and HF models. It can be seen that the local optimal is in a similar location in the design space, and the value of σ_T is within 0.3 K, show that a LF approach with 10 times less computational cost is suitable for this particular problem.

Note that this 2D optimisation study can be used on an existing nozzle in the CRESU community. For instance, a large range of pressure can be analysed, and the best operating pressures in terms of σ_T can be used to perform pressure dependent kinetics. This feature has been implemented into the existing code and has been used by the University of Birmingham, and will be a part of the code improvement in future studies.

2. *Multi Objective Optimisation*

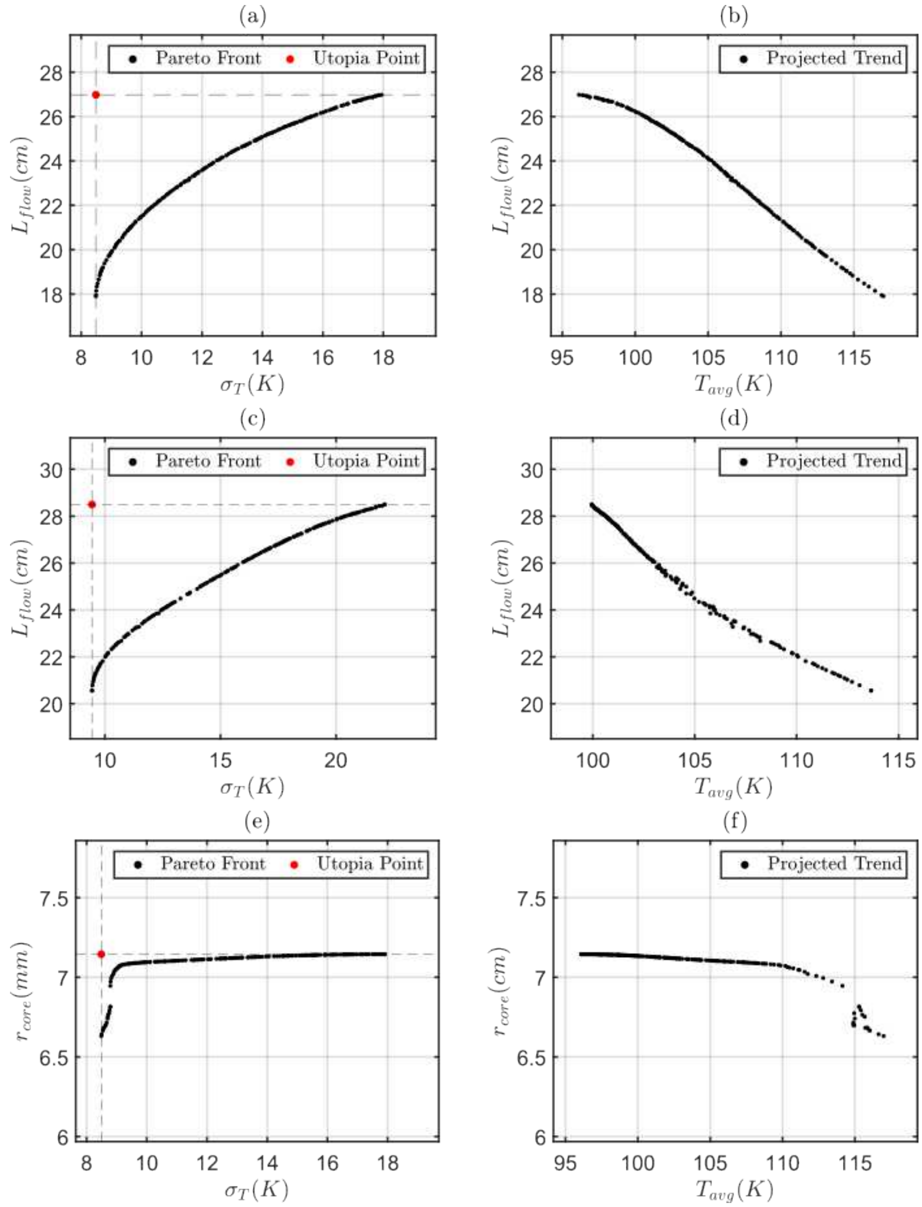

FIG. 3. Multi objective optimisation of σ_T and L_{flow}, where (a) shows the Pareto front, and (b) is a projection of the optimal values onto the L_{flow} and T_{avg} design space. Subplots (a) and (b) refer to the Pareto from obtained with the low fidelity model, and (c) and (d) refer to the Pareto from obtained with the high fidelity model. Plots (e) and (f) show the Pareto front using r_{core} and σ_T multi objective results using the low fidelity model.

Alt Text: Six Scatter plots of the multi objective Pareto front found using the low fidelity and high fidelity approaches. The flow uniformity decreases with an increase in flow length, and the flow length decreases with an increase in temperature.

A multiobjective optimisation study was also conducted, minimising σ_T and maximising L_{flow} to understand the dependencies of the constraints and objective functions for supersonic jets. The mathematical formulation is given in Equation 14. Here f_1 and f_2 correspond to the two objectives. It should be noted that f_2 has been multiplied by -1 to convert the maximisation objective into a minimisation problem.

$$\begin{aligned}
& \mathbf{x} = [x_1, x_2]^n \quad \text{where, } n = 1, 2, ...N \\
\textbf{Minimise} \quad & f_1(\mathbf{x}) = \sigma_T(\mathbf{x}) \\
& f_2(\mathbf{x}) = -L_{flow}(\mathbf{x}) \\
\textbf{Subject to} \quad & g_1(\mathbf{x}) = 15cm - L_{flow}(\mathbf{x}) \leq 0 \\
\textbf{where:} \quad & 4000 \text{ Pa} \leq x_1 \leq 6000 \text{ Pa} \\
& 100 \text{ Pa} \leq x_2 \leq 200 \text{ Pa}
\end{aligned} \tag{14}$$

Figure 3a and 3c show the Pareto front from the optimisation problem for the LF and HF models, respectively, and Figure 3b and 3d compare the second objective to the average temperature of the jet. It can be seen that both the low-fidelity (LF) and high-fidelity (HF) models exhibit the same Pareto front structure, which follows a logarithmic trend. There is a clear trade-off between σ_T and L_{flow}, where increasing L_{flow} results in a corresponding increase in σ_T, and vice versa.

From a design perspective, it may be advantageous to balance a small increase in σ_T in exchange for a significant gain in L_{flow}. For example, as shown in Figure 3a, an increase in σ_T of only 0.5 K (from 8.5 K to 9.0 K) can yield an increase in flow length of nearly 10%. This flexibility is particularly useful when selecting suitable operating conditions, allowing them to target a specific flow length to meet kinetic requirements. This trade-off is especially valuable in pulsed systems, where physical constraints on nozzle size and pumping capacity may limit the achievable flow length.

3. *Dynamic Pressure Bounds*

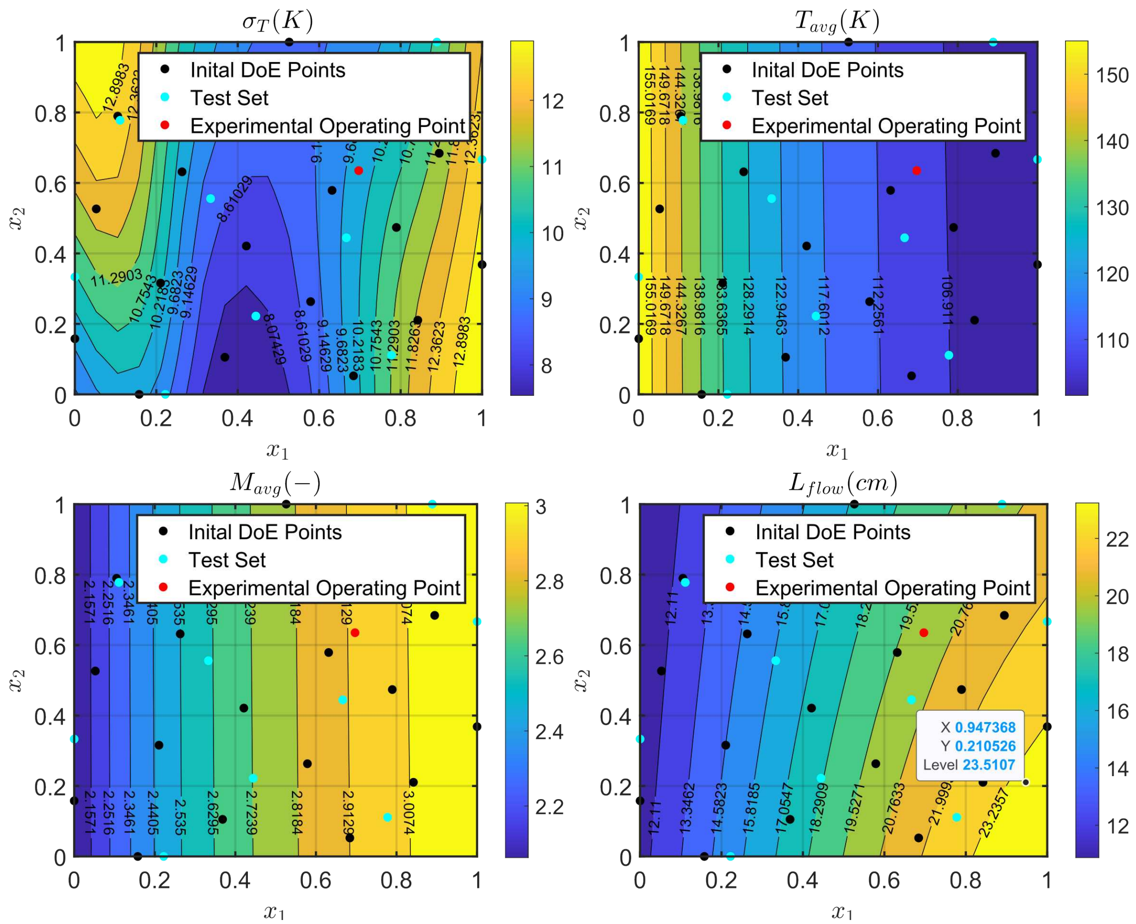

FIG. 4. 2D contours of σ_T, T_{avg}, M_{avg}, L_{flow} and r_{core} The optimal hyper parameters (ϕ_1,ϕ_2, λ) for each model are σ_T = (-1.10, -9.97, $1 \cdot 10^{-5}$), T_{avg} = (0.99, -0.29, $1 \cdot 10^{-5}$), M_{avg} = (0.76, 9.91, $3.97 \cdot 10^{-2}$), L_{flow} = (0.21, 0.75, $1 \cdot 10^{-5}$) and r_{core} = (1.51, -6.53, $1 \cdot 10^{-5}$).

Alt Text: Response surface plots of flow uniformity, jet temperature, jet Mach number and flow length, overlaid with a scatter plot of the initial design of experiments and test set.

The preceding pressure study relies either on prior knowledge to define inlet pressure bounds or on exploration of a large design space to assess the influence of operating pressure for a fixed nozzle geometry. To remove this requirement, a dynamic inlet pressure bound was introduced. This outlet pressure range can be defined according to the requirements of a specific CRESU apparatus, thereby providing a flexible framework for investigating the impact of operating pressure on arbitrary nozzle geometries without the need to prescribe explicit inlet pressure bounds.

The scaling is based upon the 1D isentropic relationships, although they will be shown again here for continuity. The area ratio of the nozzle can be used to calculate the Mach number of the jet at the nozzle exit:

$$\frac{A}{A^*} = \left(\frac{\gamma+1}{2}\right)^{\frac{\gamma+1}{2(\gamma-1)}} \frac{1}{M}\left(1+\frac{\gamma-1}{2}M^2\right)^{\frac{\gamma+1}{2(\gamma-1)}} \tag{15}$$

where A in this case is the nozzle exit area, and A^* is the throat area, calculated using the area of a circle. The isentropic pressure ratio between the reservoir (P_1) and jet flow (P_2) can be calculated from the Mach number using:

$$PR = \frac{P_1}{P_2} = (1+\frac{\gamma-1}{2}M^2)^{\frac{-\gamma}{\gamma-1}}, \tag{16}$$

Which allows the operating pressure of the reservoir to be estimated with the vacuum chamber pressure, assuming ideal flow using:

$$P_{res} = \frac{1}{PR}P_{chm} \tag{17}$$

where P_{res} is the reservoir pressure, P_{chm} is the chamber pressure, which can be set based on the vacuum pressures available for a specific CRESU apparatus. The M2.25 nozzle was used with nitrogen as a bath gas, and the inlet and outlet pressure boundary conditions were parametrised. Again the M2.25 nozzle was used as a baseline case, and a LF mesh approach was adopted. The area ratio for the M2.25 was 4.70 based on the throat and nozzle exit radius, and the PR based on Equation 15 was 43.29. The single objective optimisation formulation for this problem with the scaling factor is as follows:

$$\begin{aligned}
& \mathbf{x} = [x_1, x_2]^n \quad \text{where } n = 1, 2, ..., N \\
\textbf{Minimise} \quad & f_1(\mathbf{x}) = \sigma_T(\mathbf{x}) \\
\textbf{Subject to} \quad & g_1(\mathbf{x}) = 13\text{ cm} - L_{flow}(\mathbf{x}) \leq 0 \\
\textbf{where:} \quad & (1+0.2PR)x_2 \leq x_1 \leq PRx_2 \\
& 100\text{ Pa} \leq x_2 \leq 200\text{ Pa}
\end{aligned} \tag{18}$$

The resulting surrogate models are shown in Figure 4. This shows a central region of low σ_T, indicating that a range of operating pressures can produce a uniform flow for a given nozzle geometry.

Model	$\mathbf{x}^* = (x_1, x_2)$	$\sigma_T(\mathbf{x}^*)$ (K)	$T_{avg}(\mathbf{x}^*)$ (K)	$L_{flow}(\mathbf{x}^*)$ (cm)
LF Kriging Prediction	[0.4103 0]	7.532	120.32	18.23
LF CFD Evaluation	[0.4103 0]	7.647	119.81	17.91
HF CFD Evaluation	[0.4103 0]	8.797	119.29	20.09

TABLE III. Comparison of Kriging model predictions compared with LF and HF CFD calculations at the optimal location for the 2D scaled pressure study.

Alt Text: Evaluation of global optima, where the flow length, average jet temperature and flow length are compared.

Results from a representative optimisation study minimising σ_T are summarised in Table III. The close agreement in σ_T between the dynamically constrained pressure bounds and the previous two-dimensional shape study demonstrates the effectiveness of this approach in identifying optimal operating pressures.

In this, the reservoir pressure bounds (x_1) are scaled based on the isentropic pressure ratio and the vacuum pressure (x_1). The flow length constraint was reduced from 15 cm to 13 cm, as the LF generally predicts the flow length within 2 cm compared to the HF model, as shown in Table III. Note that an additional x_2 was added to the lower bound of x_1 to enforce that $x_1 > x_2$ for any nozzle used, ensuring a positive pressure ratio across the nozzle at all times.

B. 2D Shape Study

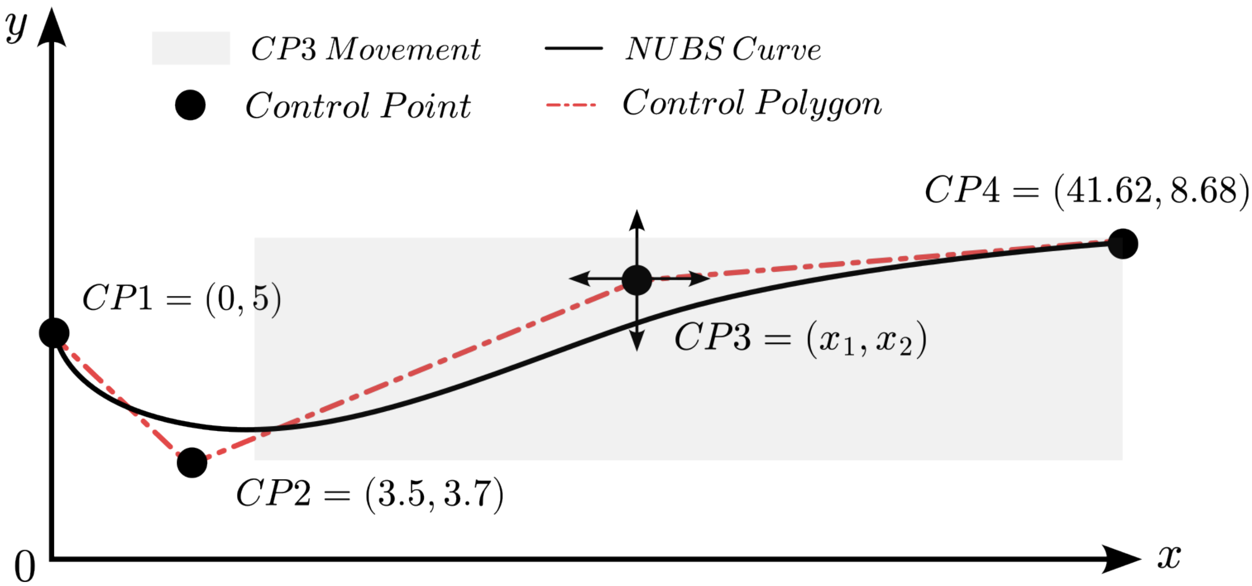

FIG. 3. Schematic of Laval nozzle parametrisation in the 2D shape study, where CP refers to the control points. The shaded grey area represents the possible movement of $CP3$. The positions of $CP1$, $CP2$ and $CP4$ are based on the original M2.25 nozzle designed using the MOC.

Alt Text: Drawing showing an example Laval nozzle, with the locations of the four control points and their horizontal and vertical movement used to parametrise the Laval nozzle using a NURBS curve.

To understand the relationship between the control points used to define the NUBS curve which describe the Laval nozzle profile, a 2D optimisation study was conducted by varying a single control point. The nozzle was again based on the existing M2.25 as a basline for comparison. In this study, a low fidelity meshing approach was used, with the optimisation framework in the main text. The Laval nozzle geometry was parametrised using a NUBS curve, with four control points denoted (CP) as shown in Figure 3, where each control point is essential for an important aspect of the nozzle shape (e.g. throat, curvature, length and exit radius).

Here the control points $CP1$, $CP2$ and $CP4$ are static, and have been set based to match the inlet radius, throat diameter, nozzle exit diameter and nozzle length of the M2.25 nozzle. The control point $CP3$ can move both horizontally and vertically to alter the curvature of the diverging section, where the position is controlled by each design dimension. Note that the M2.25 nozzle can be approximately recovered when $CP3(x_1, x_2) = (24{,}7)$. Therefore, the two dimensional single objective shape optimisation problem can be formulated as follows:

$$
\begin{aligned}
& \mathbf{x} = [x_1, x_2]^n \quad \text{where, } n = 1, 2, ...N \\
\textbf{Minimise} \quad & f_1(\mathbf{x}) = \sigma_T(\mathbf{x}) \\
\textbf{Subject to} \quad & g_1(\mathbf{x}) = 13cm - L_{flow}(\mathbf{x}) \leq 0 \\
\textbf{where:} \quad & 4\,\text{mm} \leq x_1 \leq 40\,\text{mm} \\
& 4\,\text{mm} \leq x_2 \leq 8.68\,\text{mm}
\end{aligned}
\tag{19}
$$

where again σ_T is to be minimised across the design space, with a constraint requiring the minimum flow length to 13 cm, and the horizontal movement (x_1) ranges from 4 - 40 mm, and the vertical movement ranges from 4 - 8.88 mm. The upper bound of x_2 does not exceed the nozzle exit diameter to ensure Laval nozzle type geometries are always created, and no internal bulges are present.

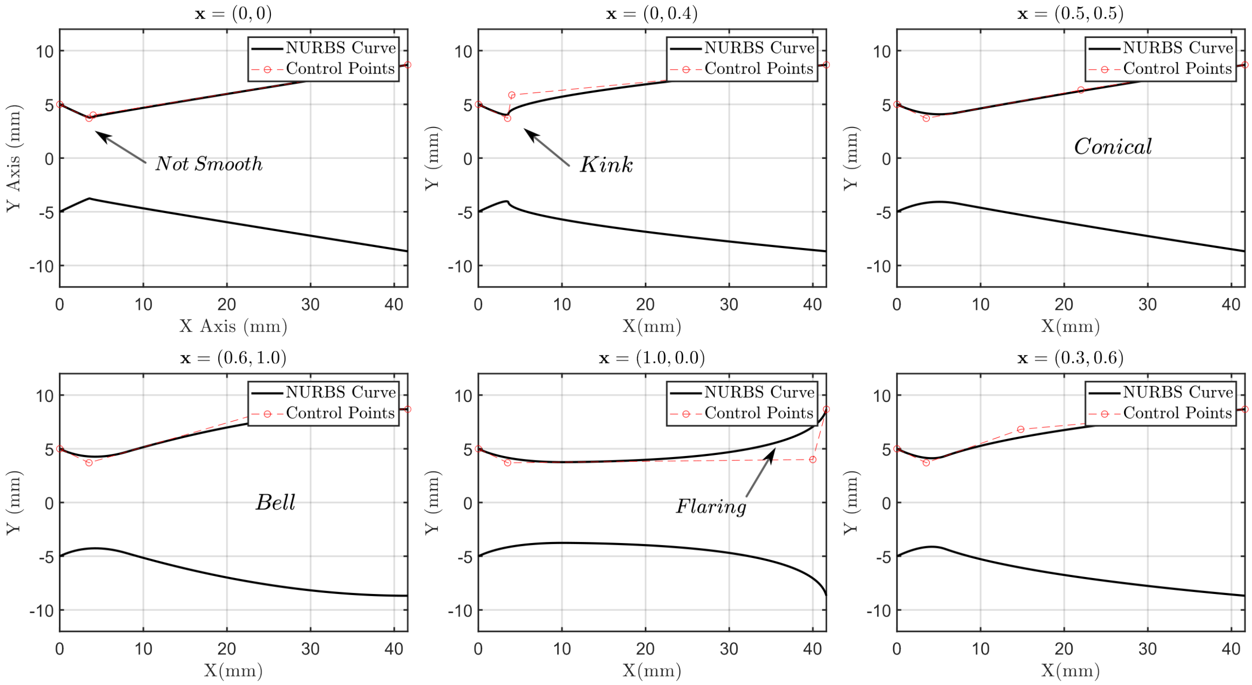

FIG. 4. Comparison of NUBS curves created using different values of $\mathbf{x}$, the corresponding kinetic parameters of interest for each of the nozzles is shown in Figure 5

Alt Text: Six plots showing how the Laval nozzle geometry changes across the design and a control point is moved, highlighting that many regions are non-optimal and can be ignored.

A comparison of the metamodels for each parameter generated for this study is shown in Figure 5. There are two regions of the σ_T design space that are optimal for kinetics, these occur at approximately $x^* = (0,\ 0.4)$ and $x^* = (0.6,\ 1)$. Even though the σ_T is low in the case where $x^* = (0,\ 0.4)$, it can be seen that there is a kink in the geometry near the throat of the nozzle as the control point CP3 is too close to CP2. A kink in the geometry causes shocks to form in the nozzle, and hence artificially reduces σ_T in the post nozzle regions, and reduces L_{flow} in comparison to a bell shaped nozzle in the other region where $x^* = (0.6,\ 1)$. Depending on the metamodel creation, during optimisation it can fall in the region where there are kinks present in the geometry, which is not useful for kinetics studies, and would be significantly harder to manufacture than a smooth nozzle. Furthermore, nozzles that are not either conical or bell in shape perform extremely badly in terms of σ_T as the expansion rate is too fast, for example $x^* = (1.0,\ 0)$, hence this region of the design space can be removed during the search.

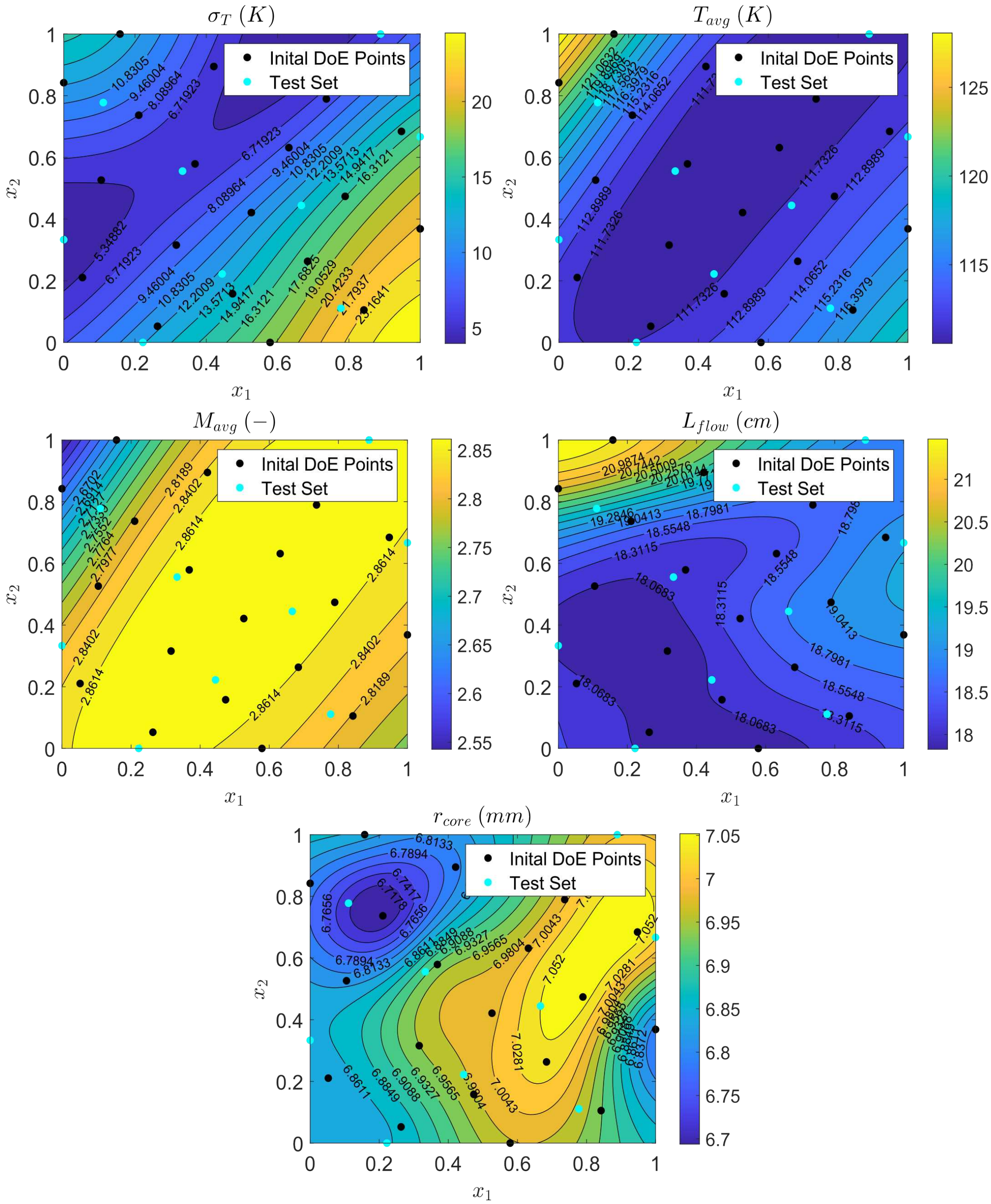

FIG. 5. 2D contours of σ_T, T_{avg}, M_{avg}, L_{flow} and r_{cpre}. Note that the distance hyper parameters are in log scale. The test set used to calculate MAE and R^2 of the Kriging model are shown in cyan.

Alt Text: Response surface plots of flow uniformity, jet temperature, jet Mach number, flow length and core thickness overlaid with a scatter plot of the initial design of experiments and test set.

Figure 5 shows the Kriging model design space for the 2D shape study, showing there is two optimal regions, although to ensure that only converging nozzles are created with no kinks, a dynamic bound has been added to account for this.

1. *Dynamic Shape Bounds*

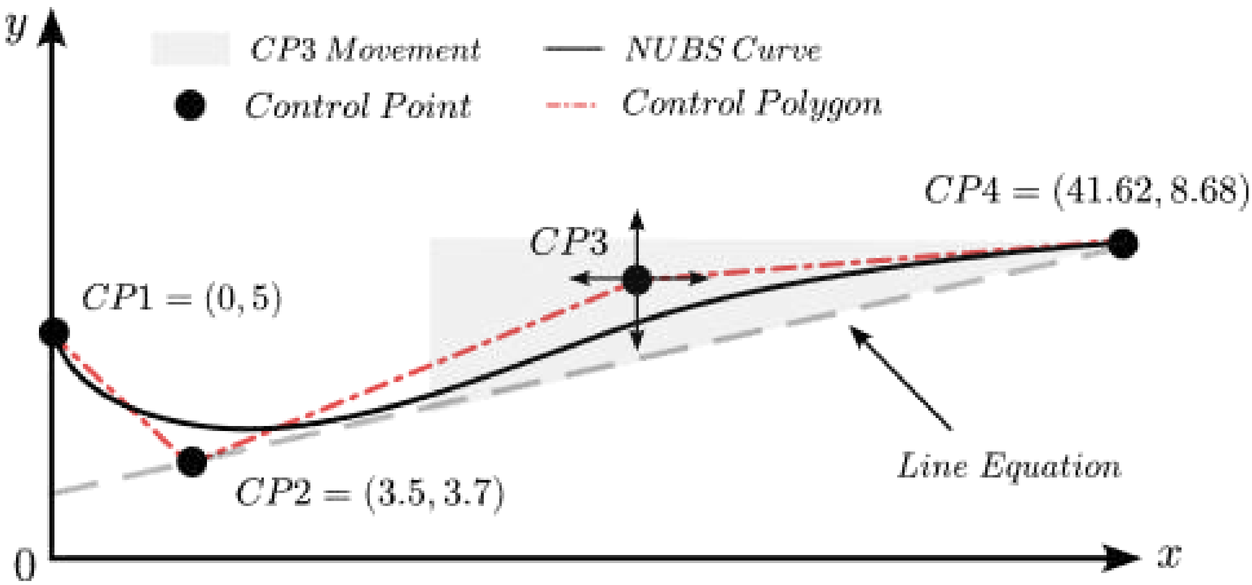

FIG. 6. Schematic of Laval nozzle parametrisation used in the 2D shape scaled study, where CP refers to the control points. The shaded grey area represents the possible movement of $CP3$. The positions of $CP1$, $CP2$ and $CP4$ are based off the original M2.25 nozzle designed using the MOC.

Alt Text: Drawing showing an example Laval nozzle, with the locations of the four control points and their horizontal and vertical movement used to parametrise the Laval nozzle using a NURBS curve.

As it is now known that there is a dependency between the NURBS control points, and geometric features of the nozzle, a variable bound can now be implemented to reduce the design space. This study employs the same control point locations for $CP1$, $CP2$, and $CP4$ as shown in Figure 6, where the control points are utilised with NUBS to generate the Laval nozzle geometry. In this, $CP3$ again can move vertically and horizontally. The horizontal movement is based on the length of the nozzle. The horizontal movement of $CP3$ is defined relative to the nozzle length, ranging from $0.3L_{nozzle}$ to $0.95L_{nozzle}$. The lower bound is set $0.2L_{nozzle}$ downstream of $CP2$, which defines the throat location, to avoid kinks in the geometry, while the upper bound ensures that $CP3$ does not exceed the nozzle length, to ensure a valid Laval nozzle geometry is generated using the NUBS technique.

The vertical movement of $CP3$ is defined relative to the nozzle exit diameter and the line connecting $CP2$ and $CP4$. This constraint demonstrated that flared nozzles with sudden expansions result in poor performance. The gradient of the line between $CP2$ and $CP4$ is defined as:

$$m = \frac{dy}{dx} = \frac{CP4(x_2) - CP2(x_2)}{CP4(x_1) - CP2(x_1)} = \frac{8.68 - 3.7}{41.67 - 3.5} \tag{20}$$

The gradient can then be used to find the equation of the line between the control points $CP2$ and $CP4$:

$$y = mx + c = \frac{8.67 - 3.7}{41.68 - 3.5}x + c \tag{21}$$

where any point across the line can be used to solve for the y intercept c, in this case, $CP4$ was used, where:

$$c = 8.68 - \frac{m}{41.62} \quad where, \quad y = mx + 8.68 - \frac{m}{41.62} \tag{22}$$

The equation of this line defines the lower bound for the vertical position of $CP3$, which varies according to its horizontal location. Therefore, the single objective formulation is as follows:

$$\begin{aligned}
& \mathbf{x} = [x_1, x_2]^n \quad \text{where, } n = 1, 2, ...N \\
\textbf{Minimise} \quad & f_1(\mathbf{x}) = \sigma_T(\mathbf{x}) \\
\textbf{Subject to} \quad & g_1(\mathbf{x}) = 13cm - L_{flow}(\mathbf{x}) \leq 0 \\
\textbf{where:} \quad & 0.3L_{nozzle} \leq x_1 \leq 0.95L_{nozzle} \\
& mx_1 + 8.68 - \frac{m}{41.62} \leq x_2 \leq 8.68\,\text{mm}
\end{aligned} \tag{23}$$

where m is the gradient of the line that passes through $CP2$ and $CP4$, and L_{nozzle} is the horizontal length between $CP1$ and $CP4$. This scaled approach is based on information of the design space known a priori, aiming to place points in suitable regions of the design space. Here, the reservoir and chamber pressures were set to 5203 Pa and 169.7 Pa, respectively, which correspond to the optimal operating pressure used in the experiments and Birmingham, and the bath used was nitrogen.

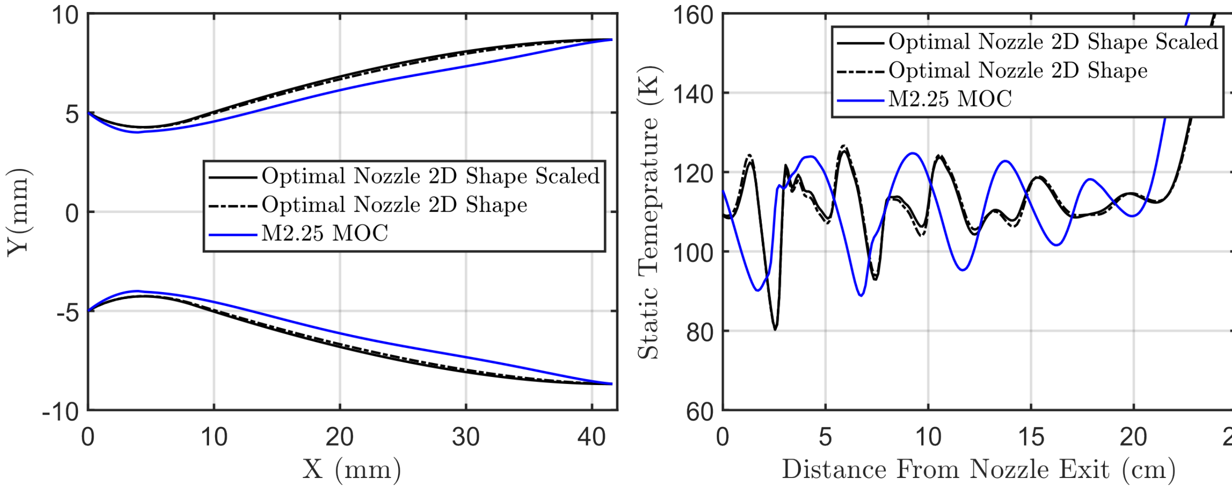

FIG. 7. Comparison between the optimal nozzle found using the 2D shape study, where (left) compares the nozzle profiles of the M2.25, optimal 2D shape study and optimal 2D scaled shape study, (right) shows the static temperature at the axis of the jet (using the HF CFD model) for each nozzle profile.

Alt Text: Line plots showing a comparison between the original Laval nozzle and optimized nozzles, with a comparison of the axial temperature profile obtained from all three Laval nozzles.

A comparison of the optimal nozzle obtained by minimising the single objective optimisation for the 2D shape study and 2D shape study with redefined bounds is shown in Figure 7. This shows that the a near identical nozzle and supersonic jet is obtained when constraining the bounds to reduce the size of the design space.

C. 4D Optimisation Study

This study combined the 2D shape and 2D pressure study with the improved formulation for the design variable bounds, which results in an optimisation problem of given in Equation 24. Here, g_1 ensures that the jet has a usable length, while g_2 and g_3 are based on manufacturing tolerances to ensure that the nozzle fits within the clamping systems used at both Leeds and Birmingham. The lower and upper bounds of the chamber pressure (x_2) were set based on the typical reservoir pressures used at both the University of Leeds and Birmingham, as this model aims to be used within both setups, as they share nearly identical nozzle sizes, and constraints can be applied based on each system's requirements.

$$
\begin{aligned}
& \mathbf{x} = [x_1, x_2, x_3, x_4]^n \quad \text{where, } n = 1, 2, ...N \\
\textbf{Minimise} \quad & f_1(\mathbf{x}) = \sigma_T(\mathbf{x}) \\
\textbf{Subject to} \quad & g_1(\mathbf{x}) = 13cm - L_{flow}(\mathbf{x}) \leq 0 \\
& g_2(\mathbf{x}) = r_{nozzle}(\mathbf{x})|_{x=19mm} - 7mm \leq 0 \\
& g_3(\mathbf{x}) = r_{nozzle}(\mathbf{x})|_{x=27mm} - 11mm \leq 0 \\
\textbf{where:} \quad & 0.3L_{nozzle} \leq x_1 \leq 0.95L_{nozzle} \\
& mx_1 + 8.68 - \frac{m}{41.62} \leq x_2 \leq 8.68\,\text{mm} \\
& (1 + 0.2PR)x_4 \leq x_3 \leq PRx_4 \\
& 20 \text{ Pa} \leq x_4 \leq 300 \text{ Pa}
\end{aligned}
\tag{24}
$$

The same optimisation framework was used at the study in the main paper, with the MIPT adaptive sampling framework untill the termination criterion was met. The final metamodel contained 440 design points using a low fidelity mesh.

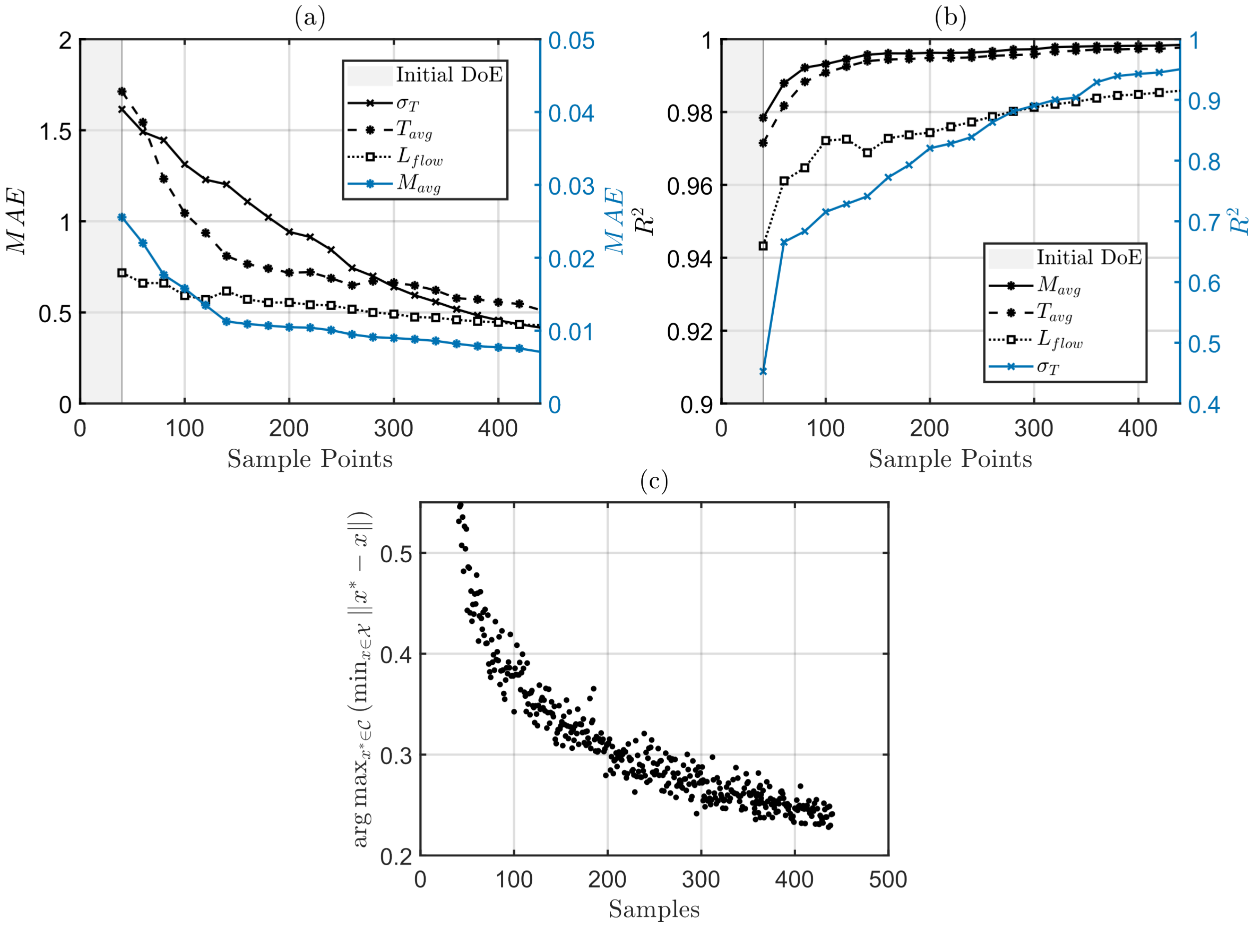

FIG. 8. Evolution of MAE with additional adaptive sampling points (a) and R^2 (b) for the 4D optimisation study. The MAE of M_{avg} and σ_T is shown on the right axis in (a) and (b), respectively, for readability. The evolution of the MIPT criterion is shown in (c).

Alt Text: Three plots showing the performance of the adaptive sampling approach for flow uniformity, jet temperature, Mach number and flow length. The first shows how the mean average error decreases with increasing sample points, the second is the correlation (R^2) and the third is how the spacing between points decreases

The evolution of the regression Kriging model error vs the test set is shown in Figure 8.The resulting regression Kriging metamodel for the low fidelity mesh using 440 samples is shown in Figure 9, with the HF models with the same design points shown in Figure 10.

Model	$\mathbf{x}^* = (x_1, x_2, x_3, x_4)$	$\sigma_T(\mathbf{x}^*)$ (K)	$T_{avg}(\mathbf{x}^*)$ (K)	$L_{flow}(\mathbf{x}^*)$ (cm)
LF Kriging	[0.5460, 0.8594,0.3737, 0.1624]	1.463	129.52	16.32
HF CFD	[0.5460, 0.8594,0.3737, 0.1624]	2.253	128.63	19.75
HF Kriging	[0.4002, 0.7547, 0.3824, 0.1756]	3.016	126.65	21.01
HF CFD	[0.4002, 0.7547, 0.3824, 0.1756]	2.370	127.55	20.87

TABLE IV. Comparison of Hf and LF Kriging model predictions compared with HF CFD calculations at the optimal location for the 4D optimisation study and the M2.25 nozzle designed using the MOC.

Alt Text: Performance evaluation of the global optimal found using the low fidelity and high fidelity meshing approaches, showing that the LF and HF models predict similar values.

A comparison between the LF and HF global optimal values and the surrogate predictions, along with the HF CFD validation for each optimal location is shown in Table IV. Both the Kriging models do not recover the exact validation values, although as the validation shows low values of σ_T, it shows that the Kriging model is accurately recovering trends seen in the data. There is some variability in the location of the optima for each case, although it should be noted that the LF approach can used to design nozzles with similar values of σ_T with reduced computational cost, hence its use for the 9D study. This justifies using the LF approach to generate the surrogates, as it is roughly ten times more computationally efficient than using the HF mesh.

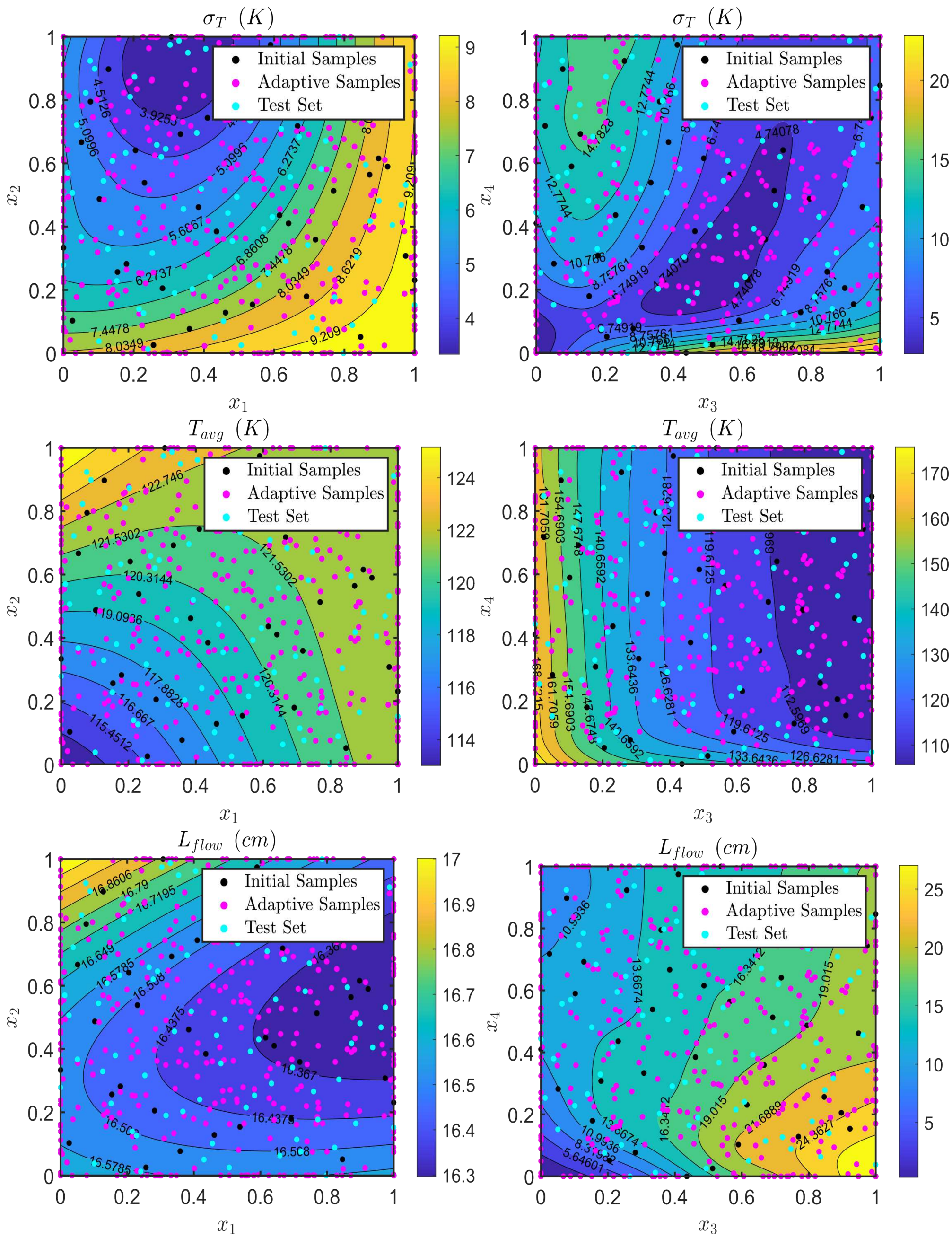

FIG. 9. Hyper-slices of the 4D LF Kriging models for σ_T, T_{avg}, and L_{flow}. The left column corresponds to $x_3 = 0.5$, $x_4 = 0.5$, and the right column to $x_1 = 0.5$, $x_2 = 0.5$.

Alt Text: Response surface plots of flow uniformity, jet temperature, and flow length for the low fidelity model, overlaid with a scatter plot of the initial design of experiments and test set.

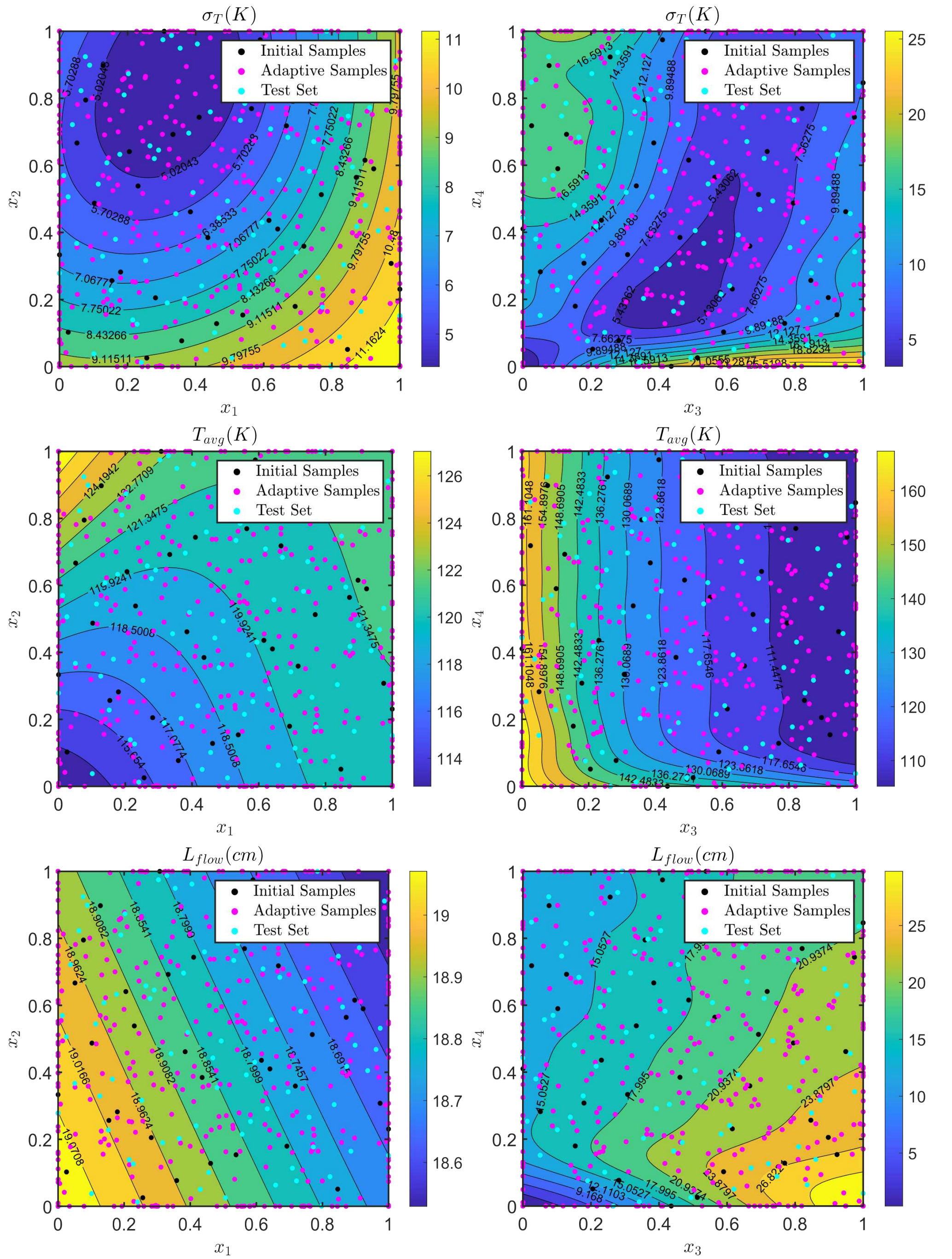

FIG. 10. Hyper-slices of the 4D HF Kriging models for σ_T, T_{avg}, and L_{flow}. The left column corresponds to $x_3 = 0.5$, $x_4 = 0.5$, and the right column to $x_1 = 0.5$, $x_2 = 0.5$.

Alt Text: Response surface plots of flow uniformity, jet temperature, and flow length for the high fidelity model, overlaid with a scatter plot of the initial design of experiments and test set.

Figure 9 and 10 shows the low fidelity and high fidelity hyper slices of the Kriging models for the 4D optimisation study, showing that the low fidelity approach can accurately recover the design space whilst being ten times less computationally expensive.

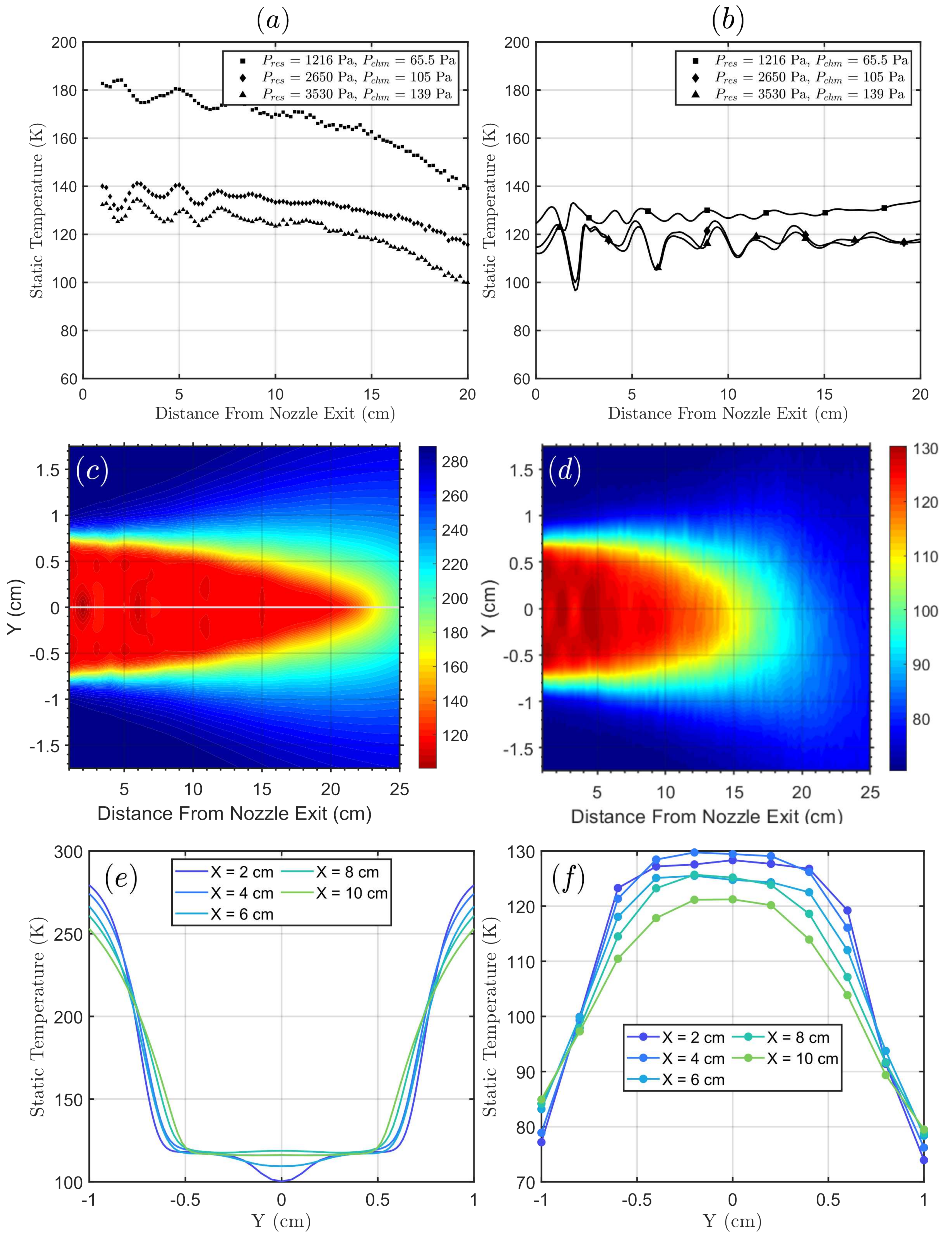

FIG. 11. Effect of operating pressure on jet flow, where (a) shows the experimental Pitot characterisation across the jet axis and (b) the CFD prediction of the static axial temperature. Subfigures (c) and (d) present the static temperature contours for the CFD and experiment, respectively, at $P_{res} = 3630$ Pa and $P_{chm} = 139$Pa. Subfigures (e) and (f) show the axial temperature across the jet for the CFD and experimental cases, respectively.

Alt Text: Comparison of axial temperature profiles from CFD and experiments at three pressures (top). 2D contours of static temperature for both experimental data and CFD predictions are shown, along with a comparison of jet core thickness between the two

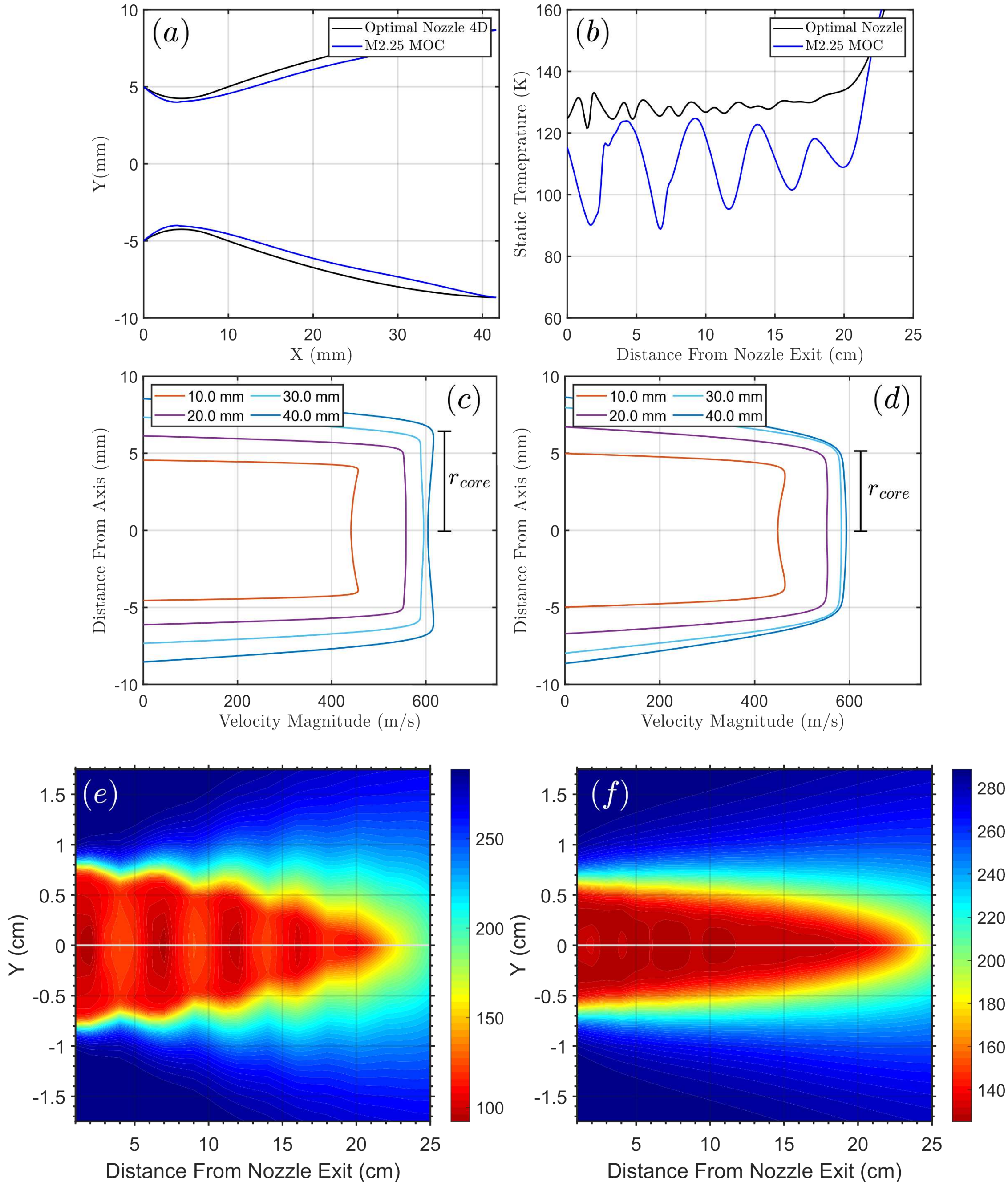

FIG. 12. Comparison between the 4D optimal nozzle and the existing M2.25 nozzle, where (a) shows the nozzle contours, (b) the axial static temperature across the jet, (c) and (d) the velocity magnitude across the internal nozzle length for the M2.25 and optimal nozzle, respectively, and (e) and (f) the static temperature contours for the M2.25 and optimal nozzle, respectively.

Alt Text: Comparison of the original and optimized Laval nozzle geometries and axial temperature profiles (top). Includes line plots of velocity profiles inside the nozzle for both cases and 2D contour plots of temperature for the respective configurations.

To improve the σ_T of the existing M2.25 nozzle, a single objective constrained optimisation was performed on Equation 24 using a genetic algorithm (GA) with a population of 100, followed by gradient descent (GD) to locally refine the GA results. The global optimum was found at $\mathbf{x}^* = (0.5460, 0.8594, 0.3737, 0.1624)$, corresponding to a physical location of $CP3$ at (26.95 mm, 8.41 mm), which is similar to the optimal placement of $CP3$ in the 2D study ($CP3$ = 28.37 mm, 8.53 mm). At this optimum, the reservoir and chamber pressures are 1216 Pa and 65.5 Pa, respectively, and $\sigma_T = 1.463$ K. The optimum is located away from the constraints, with $g_1 = -3.32$ cm, $g_2 = -0.47$ mm, and $g_3 = -3.37$ mm, all negative, indicating that all constraints are satisfied.

A comparison between the optimal nozzle and the original M2.25 nozzle is shown in Figure 12. Figure 12a presents the optimal and existing M2.25 nozzle profiles, while Figure 12b illustrates the axial static temperature across the jet. Figures 12c and 12d show the velocity magnitude along the nozzle length for the M2.25 and optimal nozzles, respectively. Finally, Figures 12e and 12f present the temperature contours of the jets for the M2.25 and optimal nozzles, respectively. The optimal nozzle is a bell-type nozzle, is recovered, demonstrating the capability of both the scaled approach and the adaptive sampling based regression Kriging framework when applied to a higher-dimensional problem. The BL growth along the nozzle wall is significantly larger for the optimal nozzle compared to the M2.25. At a location 40 mm downstream of the nozzle inlet, the core radius r_{core} is 4.91 mm for the optimal nozzle and 6.49 mm for the M2.25. Consequently, the BL thickness of the optimal nozzle is 1.58 mm greater, corresponding to a 24% increase. This increase in boundary layer thickness arises from the nozzle curvature, where the area ratio expands more rapidly for the optimal nozzle, promoting faster boundary layer growth before the nozzle exit.

The optimal nozzle from this study alongside the operating conditions were used to validate the nozzle design. The experimental validation is seen in Figure 11.

In this the operating pressures were increased from $Pres = 1216$ Pa and $P_{chm} = 65.5$ Pa (i.e. the operating pressure from the optimisation) to $P_{res} = 3530$ Pa and $P_{chm} = 139$ Pa. It can be seen that the CFD does not correctly predict the jet temperature at low pressures. Operating at lower pressures, and hence lower densities, could potentially lead to rarefaction effects, particularly at the Pitot tube as the Kn increases due to a reduction in length scales. The local Knudsen number (Kn) for this low-pressure case was calculated, taking the nozzle throat diameter as the characteristic length and nitrogen as the working gas. The resulting Kn values in the reservoir and core flow were 0.0004 and 0.006, respectively, indicating that the jet flow remains safely in the continuum regime ($Kn < 0.01$). Note that the gradient-based Kn was also calculated, giving a maximum $Kn_{GLL} = 0.005$ which occurs across the shockwave in the jet, although, again the jet is the continuum regime. Therefore, there is limit in either the ability of the CFD to predict supersonic jets at these pressures, or potentially the experiments are more sensitive at lower pressures, and more work needs to be conducted to come to a definitive conclusion.

V. PITOT DATA TRANSFORMATION

This section contains the RAW data from the Pitot results for each of the nozzles designed in this work. As the Rayleigh-Pitot equation is invalid outside the core due to the equation assumptions, it can be hard to a direct comparison to CFD results. Therefore a linear transformation approach was used to transform the data to provide a better physical representation of the supersonic jet obtained via experiments.

A. Raw Experimental Data

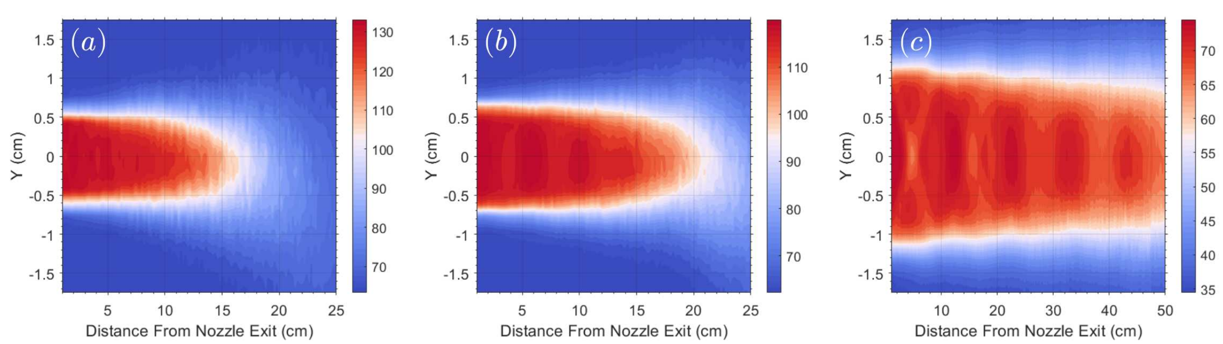

FIG. 13. Raw temperature data obtained using Rayleigh-Pitot and adiabatic relationships for the (a) 130 K, (b) 110 K, and (c) 70 K nozzles.

Alt Text: Three 2D contour plots of the raw experimental flow temperature obtained using a Pitot tube for the 130 K, 110 K and 70 K nozzles.

Figure 13 presents the raw measurements obtained by converting the impact pressure to Mach number using the Rayleigh–Pitot equation, and subsequently to temperature via the adiabatic flow relations. It is evident that the inferred temperature outside the jet core decreases toward absolute zero—a non-physical result. This behaviour arises because the Rayleigh–Pitot equation is not valid outside the core region, where its underlying assumptions break down

To transform the raw experimental data into the main dataset presented in the paper, we first assume that the temperature measured far from the nozzle (i.e., in the freestream region of the experiment) is equal to the ambient temperature predicted in the CFD simulations, which is 293 K. This assumption is physically reasonable because, in reality, the jet mixes with the surrounding chamber gas, and the temperature should asymptotically approach the ambient value rather than decrease. By enforcing this far-field temperature condition, we correct for the non-physical behaviour introduced by applying the Rayleigh–Pitot equation outside the core region.

Alongside the ambient temperature, we also use the T_{avg} of the experimental jet in the stable core region L_{flow} for each of the jets to perform a linear transformation of the temperature.

This is achieved using the following relationship

$$T_{\text{corrected}}(x,y) = \begin{cases} T_{\text{avg}} + (T_{\text{avg}} - T(x,y))\dfrac{293 - T_{\text{avg}}}{T_{\text{avg}} - T_{\text{min}}}, & T(x,y) < T_{\text{avg}}, \\ \\ T(x,y), & T(x,y) \geq T_{\text{avg}}. \end{cases} \tag{25}$$

where if the temperature of the jet $T(x,y)$ is lower than T_{avg}, we perform a linear transformation of the data towards ambient conditions using T_{avg} and the minimum temperature in the experiments (T_{min}) which is equivalent to 293 K. This criterion is valid outside the core region, and if the temperature of the jet is greater or equal to T_{avg}, the jet temperature remains the same as the raw experimental data. Note that there may be some artifacts from this approach, although the temperature of the BL when comparing experiments and CFD predictions shows very good agreement, and may be useful when determining the jet temperature for kinetic studies over using the raw data,which shows a non-physical temperature outside the core.

REFERENCES

[1]M. D. Morris and T. J. Mitchell, "Exploratory designs for computational experiments," **43**, 381–402.

[2]H. Liu, Y.-S. Ong, and J. Cai, "A survey of adaptive sampling for global metamodeling in support of simulation-based complex engineering design," **57**, 393–416.

[3]A. I. J. Forrester, A. Sóbester, and A. J. Keane, *Engineering Design via Surrogate Modelling: A Practical Guide*, 1st ed. (Wiley).

[4]M. R. Kianifar and F. Campean, "Performance evaluation of metamodelling methods for engineering problems: towards a practitioner guide," Structural and Multidisciplinary Optimization **61** (2020), 10.1007/s00158-019-02352-1.

[5]A. I. Forrester, A. Sóbester, and A. J. Keane, "Multi-fidelity optimization via surrogate modelling," **463**, 3251–3269 ().

[6]I. Couckuyt, A. Forrester, D. Gorissen, F. De Turck, and T. Dhaene, "Blind kriging: Implementation and performance analysis," **49**, 1–13.

[7]I. Couckuyt, F. Declercq, T. Dhaene, H. Rogier, and L. Knockaert, "Surrogate-based infill optimization applied to electromagnetic problems," International Journal of RF and Microwave Computer-Aided Engineering **20**, 492 – 501 (2010).

[8]M. T. Hagan, H. B. Demuth, M. H. Beale, and O. D. Jesús, *Neural Network Design*, 2nd ed. (Martin Hagan, 2014).

[9]D. W. Marquardt, "An algorithm for least-squares estimation of nonlinear parameters," Journal of the Society for Industrial and Applied Mathematics **11**, 431–441 (1963), https://doi.org/10.1137/0111030.

[10]M. A. Ganaie, M. Hu, A. K. Malik, M. Tanveer, and P. N. Suganthan, en"Ensemble deep learning: A review," Engineering Applications of Artificial Intelligence **115**, 105151 (2022), arXiv:2104.02395 [cs].

[11]L. Driver, K. Douglas, D. I. Lucas, T. Guillaume, J. H. Lehman, N. Kapur, D. E. Heard, and G. N. De Boer, "Developing a predictive model for low-temperature laval nozzles with applications in chemical kinetics," **36**, 076128.